INL/EXT-17-43415 Rev. 0

September 2017

Model Development in MARMOT for High Burn-up Structure Formation

K. Ahmed
Y. Zhang
D. Schwen
X. Bai[*]
C. Permann

Idaho National Laboratory

INL/EXT-17-43415 Rev. 0

Model Development in MARMOT for High Burn-up Structure Formation

K. Ahmed
Y. Zhang
D. Schwen
X. Bai[*]
C. Permann

September 2017

Idaho National Laboratory
Fuel Modeling and Simulation Department
Idaho Falls, Idaho 83415

[*]**Virginia Polytechnic Institute and State University**
Department of Materials Science and Engineering
Blacksburg, VA

Prepared for the
U.S. Department of Energy
Office of Nuclear Energy
Under U.S. Department of Energy-Idaho Operations Office
Contract DE-AC07-99ID13727

ABSTRACT

A phase field model for the formation of High Burn-up Structure (HBS) was developed and implemented in MARMOT. The model takes into consideration the chemical energy of gas atoms, interfacial energies of grain boundaries and bubble surfaces, and strain energy associated with dislocations, which renders the model capable of simulating the concurrent formation and growth of both bubbles and sub-grains. Moreover, in contrast to existing phase-field models of recrystallization, the current model makes no ad hoc or a priori assumptions for the nucleation rate or recrystallized grain size and shape. All the model parameters were quantified in terms of thermodynamic and kinetic properties. The model predicts a strong effect of magnitude and distribution of dislocation density, grain boundary energy, and bubble surface energy on the formation of sub-grains. The model results are shown to be consistent with theoretical predictions. For polycrystalline UO_2 at 1200K, preliminary results suggest an averaged recrystallized grain size of 0.6-1.3 microns at a critical dislocation density in the range of $\rho = 9\times10^{15} - 1.2\times10^{16}$ m^{-2}, which corresponds to a burn-up of 98-105 GWD/tU. These values lie well within the range of reported data in literature. The model will be further refined to perform mesoscale simulations for HBS formation with the purpose of developing materials models to be used in the engineering scale fuel performance modeling. This work is supported by the DOE Nuclear Energy Advanced Modeling and Simulation (NEAMS) program.

Table of Contents

1. Introduction

For economic reasons and in anticipation of the operating conditions of next generation reactors, nuclear fuels have been continuously tested at high burn-up conditions (>40GWD/tM). Most of these tests have reported the formation of the so-called high burn-up structure (HBS) [1-10]. The HBS exhibits a porous, fine-grained microstructure as opposed to the as fabricated dense, coarse-grained microstructure. Initially, the HBS was called the *rim structure* due to its confinement to the periphery of the fuel pellet in light water reactors (LWRs), where it was observed first [1-8]. A micrograph that captures the formation of HBS in UO_2 fuel pellet is shown in Fig. 1. As evident from the figure, HBS forms at the rim region of the pellet. This is due to the higher burn-up and lower temperature in this region. The burn-up value at the periphery could be twice as large as in the pellet center as reported in Fig. 2. This is caused by the presence of higher Pu concentration resulting from resonance absorption of epithermal neutrons by U^{238} [1, 3]. Large variations of porosity and lattice parameter also develop across the fuel pellet as demonstrated in Fig. 2. Nonetheless, in heterogeneous fuels such as MOX and others, the restructuring is no longer confined to the rim region and instead spreads into different places with high enough local burn-up [8, 9]. That observation pushed the community to abandon the old term *rim structure* in favor of the more general term *high burn-up structure*.

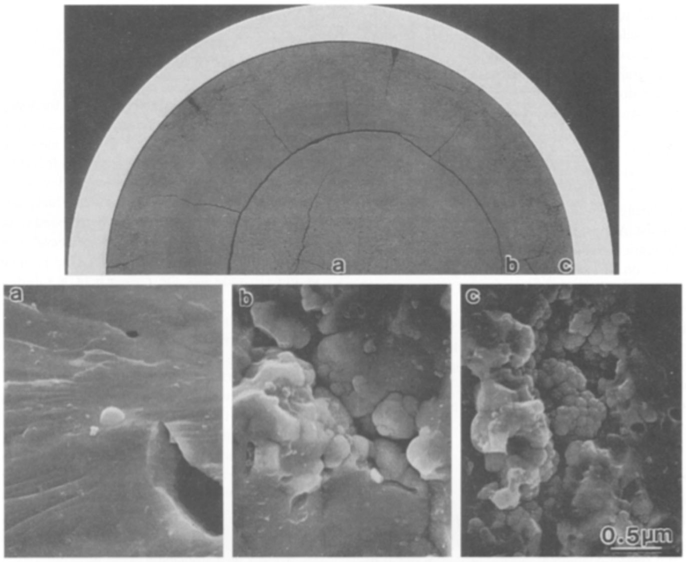

Fig.1. A micrograph of standard fuel pellet exhibiting the formation of high burn-up structure (HBS) [2].

The most likely driving force for HBS formation is the reduction of the strain energy by introducing defect-free new sub-grains at the expense of damaged/deformed grains [1-10]. This reduction offsets the increase of interfacial energy due to the formation of new boundaries. Other possible driving forces include the segregation and precipitation of fission products, including both gases and solid fission products. While the community has to some degree reached a consensus on the driving force for HBS formation, the mechanism by which it proceeds is still debatable [1]. Different hypotheses and theories were introduced to explain the phenomenon [8, 9, 11-15]. The main suggested mechanisms are recrystallization and grain subdivision driven by the strain energy [1-15]. In the recrystallization scenario, new sub-grains nucleate and then grow at the expense of damaged grains, i.e., grains with high dislocation densities caused by radiation. For the case of grain subdivision, It is proposed that the spatial rearrangement of networks dislocations into small angle boundaries leads eventually to the division of original large grains into smaller sub-grains.

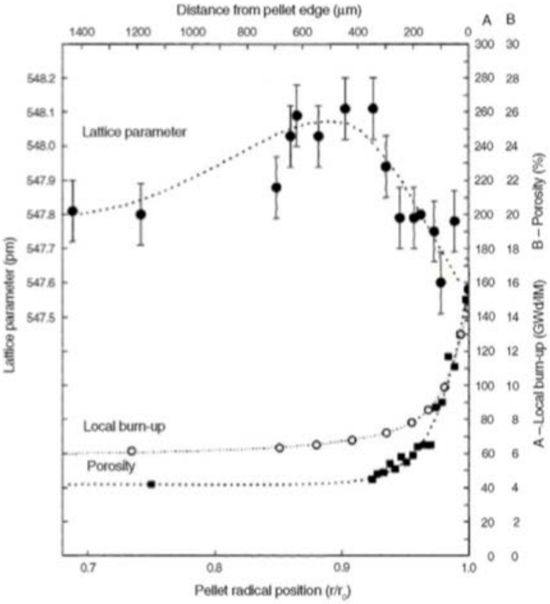

Fig. 2. Variation of lattice parameter, porosity and local burn-up across the fuel pellet [1].

In some situations, the mechanism of HBS formation seems clearer. For instance, in most metallic fuels, the recrystallization scenario seems more plausible since most of the newly formed grains in these systems are usually observed in the vicinity of original grain boundaries and have high angle boundaries. This is captured in Fig. 3, which shows the recrystallization of new sub-grains in U-Mo metallic fuel. As evident from the figure, the new sub-grains tend to form close to the grain boundaries of original grains and then spread into the bulk as the fission density increases. It is also clear from the figure that a threshold value for the fission density exists below which no HBS is observed.

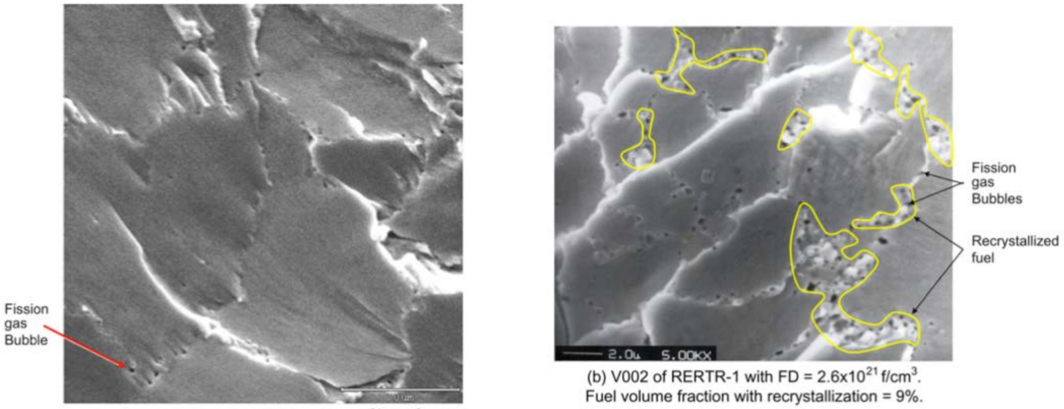

(a) V07 of RERTR-3 with FD = 2.0×10^{21} f/cm^3.
Fuel volume fraction with recrystallization = 0%.

(b) V002 of RERTR-1 with FD = 2.6×10^{21} f/cm^3.
Fuel volume fraction with recrystallization = 9%.

Fuel volume fraction with recrystallization = 9%.

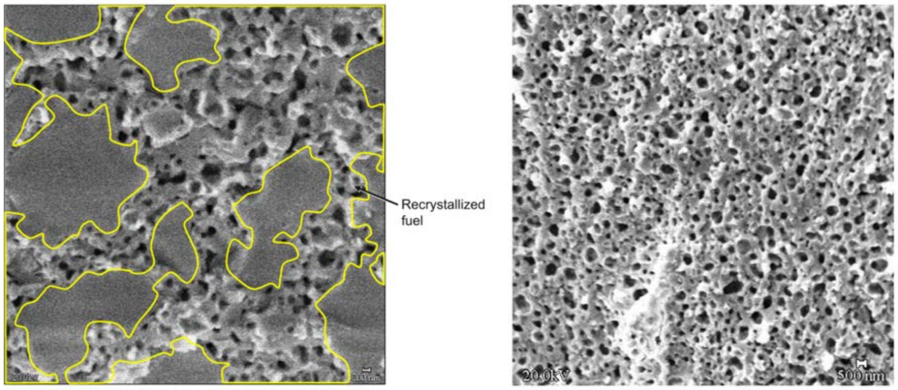

(c) V6001M of RERTR-4 with FD = 4.8×10^{21} f/cm^3.
Fuel volume fraction with recrystallization = 65%.

(d) V6022M of RERTR-4 with FD = 5.6×10^{21} f/cm^3.
Fuel volume fraction with recrystallization = 100%.

Fig. 3. Development of high burn-up structure (HBS) in U-Mo at different fission density levels [10]. Note that there is a threshold value of fission density for HBS formation. Moreover, due to the preferential nucleation of new sub-grains close to the original grain boundaries regions, recrystallization is believed to be the mechanism by which HBS forms.

The situation, however, is more complicated for the case of ceramic fuels such as UO_2 and MOX [8, 9]. In such materials systems, there is no general agreement on the mechanism responsible for HBS formation. In the beginning, it was believed that HBS proceeds by recrystallization in UO_2 fuels. This claim was supported by the formation of sub-grains with high angle boundaries and the localization of these sub-grains to the surfaces of intra- and inter-granular bubbles as shown in Fig. 4. On the other hand, other studies reported uniform formation- not just in the vicinity of bubbles or grain boundaries- of sub-grains with low angle boundaries, which fits more in the narrative of grain subdivision [1]. Moreover, more recent investigations reported the formation of planar defects before the formation of HBS in UO_2 and MOX fuels [8, 9]. Fig. 5 demonstrates the formation of these planar defects in UO_2. It is believed that these planar defects are some type of UO_2 over-structure with smaller lattice parameter [8, 9]. It is hypothesized that the new sub-grains form at the surfaces of these planar defects that themselves eventually transform into bubbles [8, 9]. Nevertheless, the exact nature of these planar defects and the role they play in HBS formation are yet to be understood.

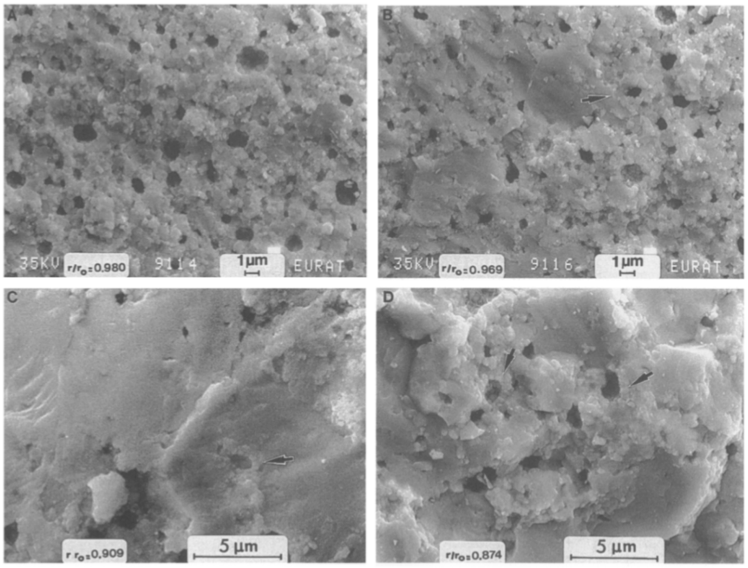

Fig. 4. Formation of HBS in UO_2 fuel pellet [3]. Note that most sub-grains are formed close to both intra- and inter-granular bubbles, which was considered to be an evidence of recrystallization.

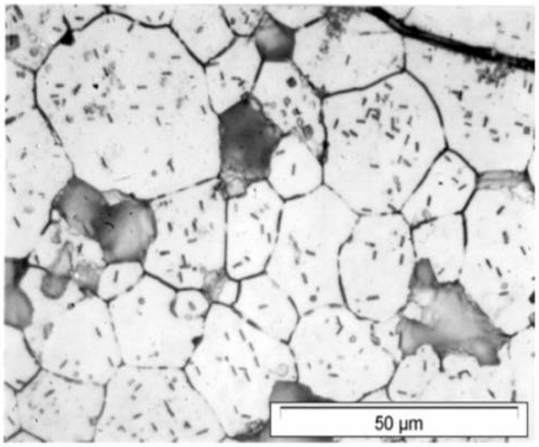

Fig. 5. Formation of planar defects before the formation of HBS in UO_2 [8]. The planar defects are believed to be some type of UO_2 over-structure with smaller lattice parameter.

The main goal of the current model development is to simulate the process of HBS formation and evolution using the phase-field method. The simulations will be used to develop engineering scale materials models for fuel performance modeling. The phase-field method is a powerful modeling approach that has been used to investigate different types of phase transformations in heterogeneous materials [16, 17], and hence it renders itself as a promising candidate for simulating HBS formation. While, as mentioned above, the detailed mechanism of HBS formation in UO_2 has not been settled yet, we assume here that the process takes place via recrystallization. There are two main reasons for our assumption. The first is the abundance of theoretical, modeling and experimental results that based their conclusions on the recrystallization scenario [2-7, 11-15], which will be used here to assess our model predictions. The second is the fact that the same model presented here can potentially be extended to simulate HBS formation in metallic fuels where recrystallization was shown to be the mechanism that facilitates HBS formation. We also want to mention that the free energy based recrystallization model developed here allows for a straightforward extension to account for fission produces as driving forces in the future. We note that the development of a comprehensive model for the complicated case of HBS formation in UO_2 will not be complete until a full understanding of the HBS formation mechanism(s) is established.

A few phase-field models of recrystallization exist in literature [18-20]. These models account for both interfacial and strain energies and hence can simulate the growth of recrystallized grains at the expense of damaged/deformed grains. However, the studies presented using these models did not simulate the nucleation stage, but instead randomly introduced circular grains as seed nuclei for recrystallization. There are two main shortcomings with this approach. First, it renders the model capable of only simulating the growth but not nucleation stage. Second, even the growth rate would be questionable since the expected shape of nuclei is not circular as seen from experiments, neither that anticipated from the principles of mechanical equilibrium. Moreover, these models do not consider the presence and/or simultaneous evolution of second-phase particles that may strongly affect both the nucleation and growth rates of sub-grains during recrystallization. This is of particular interest to the case of HBS formation since bubbles are known to have high impact on the recrystallization process. In addition, it is expected that the new boundaries of sub-grains enhance the nucleation and growth of fission bubbles, which eventually facilitates the formation of the highly porous HBS.

The phase-field model introduced here is particularly designed to alleviate the shortcomings of the existing recrystallization models discussed above. Specifically, it is used to simulate both nucleation and growth of sub-grains, and hence no a priori assumptions are used for the nucleation rate or the shape and size of the recrystallized nuclei. Moreover, the presence and evolution of bubbles are directly taken into account by tracking the production, diffusion and clustering of Xe gas atoms that result from fission events. The phase-field model developed here has been implemented in MARMOT and parameterized for UO_2.

The structure of this report is as follows. Section 2 elaborates on the construction of the phase-field model of HBS formation and growth. It also includes the details of model parameterization and numerical implementation in MARMOT. The presentation and discussion of the model results then appear in Section 3. Discussion of the limitations of the present model and future work is given in Section 4. Finally we conclude in Section 5.

2. Phase field modeling for HBS formation and evolution

2.1 Model description

The model developed here is based on a compilation of the work by Moelans et. al. on grain growth, migration of recrystallized boundaries, and formulation of thermodynamically-consistent multi-phase fields models [18, 21, 22]. Furthermore, we employ the ideas of Plapp et. al. to decouple the interfacial properties from bulk properties in a diffuse-interface description [23, 24]. This allows us to set the interface width independently from the bulk and interfacial thermodynamic properties, and hence facilitates simulating larger domains at lower computational cost.

Here, we use several order parameters to fully describe a typical HBS microstructure. In order to achieve that goal, such set of phase fields (order parameters) must be able to distinguish between three different microstructural features, e.g., deformed grains, recrystallized grains, and bubbles. We use ρ for the dislocation density where $\rho = \rho_i$ in a deformed/damaged grain and $\rho = 0$ in a recrystallized grain and inside the bubbles. A normalized gas atom concentration c is used such that it takes the value of 1 inside the bubbles and 0 inside the grains. η_{b} uniquely identifies the bubble phase such that it equals to 1 inside the bubble and 0 everywhere else. The deformed matrix grains are represented by a set of non-conserved order parameters η_{dm_i}, while the recrystallized matrix grains are represented by another set η_{rm_i}. An illustration of the usage of these phase field variables/order parameters to depict a system of deformed and recrystallized grains and bubbles is shown in Fig. 6.

Following the theory of gradient thermodynamics suitable for heterogeneous systems [16-18], the total free energy of the system is assumed here to have the form

$$F = \int f_{\text{int}} + f_{\text{b}}^{\text{Th}} \quad d^3 r \ . \tag{1}$$

In the above equation, f_{b}^{Th} is the bulk thermodynamic free energy, while f_{int} represents the interfacial free energy due to bubble (free) surfaces and grain boundaries. The interfacial free energy is given by

$$f_{\text{int}} = A\left[\begin{array}{l} 0.25+0.25(\sum_i \eta_{dm_i}^4 + \sum_i \eta_{rm_i}^4 + \eta_{\text{b}}^4) - 0.5(\sum_i \eta_{dm_i}^2 + \sum_i \eta_{rm_i}^2 + \eta_{\text{b}}^2) \\ +\gamma_{dm}\sum_i\sum_{j>i}\eta_{dm_j}^2\eta_{dm_i}^2 + \gamma_{rm}\sum_i\sum_{j>i}\eta_{rm_j}^2\eta_{rm_i}^2 + \gamma_{rdm}\sum_i\sum_j \eta_{rm_j}^2\eta_{dm_i}^2 + \gamma_b\eta_{\text{b}}^2(\sum_i \eta_{dm_i}^2 + \sum_i \eta_{rm_i}^2) \end{array}\right] + \frac{\kappa}{2}\left[\sum_i \left|\nabla\eta_{rm_i}\right|^2 + \sum_i \left|\nabla\eta_{dm_i}\right|^2 + \left|\nabla\eta_{\text{b}}\right|^2\right] \tag{2}$$

where, A, γ_α, and κ are constants that determine the surface and grain boundary energies, with α being *dm*, *rm*, and *rdm* for boundaries between *deformed* grains, *recrystallized* grains, and that between *deformed* and *recrystallized* grains, and being *b* for bubble surface, respectively. This formulation then assumes isotropic surface and grain boundary energies. Nonetheless, the model can be generalized for anisotropic cases in a straightforward manner as in regular grain growth models [21]. The bulk free energy is expressed as

$$f_{\text{b}}^{\text{Th}} = f^{\text{ch}} + g \,. \tag{3}$$

Here, f^{ch} is the chemical free energy and g is the deformed/stored strain energy associated with dislocations produced by radiation at high burn-up.

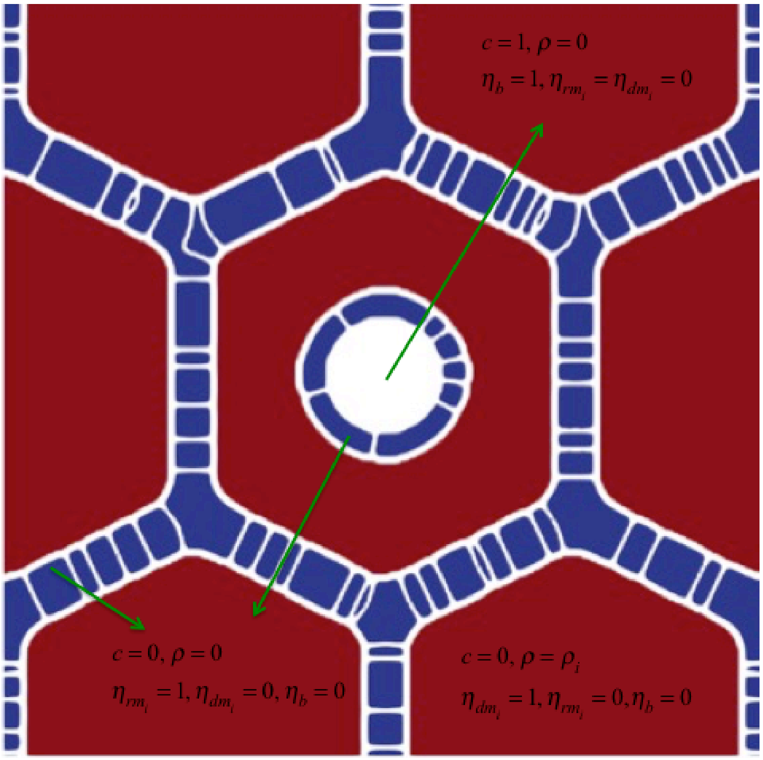

Fig. 6. An illustration of the phase fields (order parameters) used to describe the HBS microstructure. Deformed grains are shown in red, recrystallized grains are shown in blue, and grain boundaries and bubbles are shown in white. The same color scheme is followed in later presentations.

The strain energy of dislocations is given by the standard form, e.g.,

$$g(\rho_{\mathrm{eff}},\eta_1,\ldots,\eta_p)=\frac{1}{2}\mu b^2\rho_{\mathrm{eff}}\,, \tag{4}$$

where μ is the shear modulus and b is the length of the Burgers vector. The effective/average dislocation density is defined as,

$$\rho_{\mathrm{eff}}=\sum_i \rho_i h_{dm},\ \ h_{dm}=\frac{\sum\limits_i \eta_{dm_i}^2}{\sum\limits_i \eta_{dm_i}^2+\sum\limits_i \eta_{rm_i}^2+\eta_{\mathrm{b}}^2}\,. \tag{5}$$

In the above expression, ρ_i is the dislocation density in grain *i* and h_{dm} represents the fraction of deformed matrix grains in the domain. The dislocation density can vary with space and time.

A parabolic approximation of the chemical free energy of the bulk phases is used here, namely,

$$f^{ch}=B(c-h_{\mathrm{b}})^2\ \ ,\ h_{\mathrm{b}}=\frac{\eta_{\mathrm{b}}^2}{\sum\limits_i \eta_{dm_i}^2+\sum\limits_i \eta_{rm_i}^2+\eta_{\mathrm{b}}^2}\,, \tag{6}$$

where, B is a constant that sets the value of the chemical free energy and h_{b} represents the bubble fraction. This specific form eliminates any contribution of the chemical free energy to the interfacial energy [23, 24]. Note that this form assumes equal curvatures of the parabolas representing the matrix and bubble phases. This is acceptable if one assumes the bubbles have their equilibrium pressure, and hence the value of the sole curvature can be used to represent the excess free energy in the matrix due to gas atoms supersaturation. Specifically, we fix the parabola such that the chemical potential calculated from Eq. (6) approximates the exact chemical potential given by the ideal solution form, e.g.,

$$2B\bar{c}=\frac{K_{\mathrm{B}}T}{\Omega}\ln\frac{\bar{c}}{c^{\mathrm{eq}}}\,. \tag{7}$$

Here, K_B is Boltzmann constant, Ω is the atomic volume, T is the absolute temperature, $\bar{c}$ is the average gas concentration in the matrix, c^{eq} and is the equilibrium gas concentration in the matrix. The equilibrium gas concentration has the regular form, viz.,

$$c^{\mathrm{eq}}=\exp(-E^{\mathrm{f}}/K_{\mathrm{B}}T)\,, \tag{8}$$

where, E^{f} is formation energy of a gas atom.

The evolution equations for the phase fields/order parameters can be derived from the principles of irreversible thermodynamics [16, 17]. The non-conserved order parameters evolve according to Allen-Cahn equations [16-18] as

$$\frac{\partial \eta_b}{\partial t} = -L_b \frac{\delta F}{\delta \eta_b} = -L_b \left(\frac{\partial f^{\text{int}}}{\partial \eta_b} + \frac{\partial f^{ch}}{\partial \eta_b} + \frac{\partial g}{\partial \eta_b} - \kappa \nabla^2 \eta_b \right), \tag{9.a}$$

$$\frac{\partial \eta_{dm_i}}{\partial t} = -L_{dm_i} \frac{\delta F}{\delta \eta_{dm_i}} = -L_{dm_i} \left(\frac{\partial f^{\text{int}}}{\partial \eta_{dm_i}} + \frac{\partial f^{ch}}{\partial \eta_{dm_i}} + \frac{\partial g}{\partial \eta_{dm_i}} - \kappa \nabla^2 \eta_{dm_i} \right) \quad \forall i, \tag{9.b}$$

$$\frac{\partial \eta_{rm_i}}{\partial t} = -L_{rm_i} \frac{\delta F}{\delta \eta_{rm_i}} = -L_{rm_i} \left(\frac{\partial f^{\text{int}}}{\partial \eta_{rm_i}} + \frac{\partial f^{ch}}{\partial \eta_{rm_i}} + \frac{\partial g}{\partial \eta_{rm_i}} - \kappa \nabla^2 \eta_{rm_i} \right) \quad \forall i. \tag{9.c}$$

Here, L_{b} is a constant related to the bubble surface mobility, L_{dm_i} is a constant related to the boundary mobility of a deformed/damaged matrix grain, and L_{rm_i} of a recrystallized matrix grain. Using constant mobility coefficients is equivalent to the assumption of isotropic grain boundary and bubble surface mobilities. Nevertheless, the extension to the anisotropic case can be achieved by following the standard approach used before in the models of solidification and grain growth [16, 21].

The gas atom concentration is governed by a Cahn-Hilliard type diffusion equation [16, 17], e.g.,

$$\frac{\partial c}{\partial t} = \nabla \cdot M \nabla \mu + P, \tag{10.a}$$

$$\mu = \frac{\delta F}{\delta c} = \frac{\partial f^{ch}}{\partial c}. \tag{10.b}$$

In the above, M is the chemical mobility of gas atoms, μ is their chemical potential, and P is a source term representing the on-going production of gas atoms due to fission events. The chemical mobility is related to the diffusivity through

$$\frac{\partial^2 f^{ch}}{\partial c^2} M = D, \tag{11.a}$$

$$2BM = D. \tag{11.b}$$

Using a constant mobility here amounts to considering bulk diffusion to be the sole mechanism of gas atom diffusion. However, grain boundary and surface diffusion mechanisms can be added to the model as in the work of Ahmed. et. al. on grain growth in porous solids [25-28].

The effective dislocation density is prescribed according to a constitutive law. In general, the dislocation density can have both time and spatial dependence. These dependencies represent the accumulation of radiation damage and the heterogeneity of damage expected in distinct types of fuels used in different reactor types. A few rate theory models that describe the rate of accumulation of dislocations exist in literature [11-15]. However, for the sake of simplicity, we utilize here an empirical relation that calculates the average dislocation density for a given burn-up (Bu), e.g., [15]

$$\log \rho_{\mathrm{eff}} = 2.2\times 10^{-2}\,\mathrm{Bu} + 13.8\,. \tag{12}$$

The deformed grains are assumed to have this dislocation density. While recrystallized, the dislocation density is set to be zero in the newly formed grains. New dislocation build-up can be allowed using Eq. (12).

2.2 Determination of model parameters and implementation in MARMOT

The phase field model parameters are directly related to the thermodynamic and kinetic parameters of materials [18, 21]. The model parameters were determined here as follows

$$\gamma_{dm} = \gamma_{rm} = \gamma_{rdm} = 1.5\,, \tag{13.a}$$

$$(\gamma_{\mathrm{b}} / 1.5) = (\gamma_{\mathrm{s}} / \gamma_{\mathrm{gb}})^2\,, \tag{13.b}$$

$$A = \frac{3\gamma_{\mathrm{gb}}}{4\ell}\,, \tag{13.c}$$

$$\kappa = \frac{3}{4}\gamma_{\mathrm{gb}}\ell\,, \tag{13.d}$$

$$L_{\mathrm{dm}} = L_{\mathrm{rm}} = \frac{4M_{\mathrm{gb}}}{3\ell}\,, \tag{13.e}$$

$$L_{\mathrm{b}} = 10\frac{D}{B\ell^2}\,. \tag{13.f}$$

In the above, ℓ is the diffuse interface width, γ_{gb} is the grain boundary energy, γ_{s} is the surface energy, and M_{gb} is the grain boundary mobility. As can be deduced from Eq. (13), it is assumed here that the recrystallized and deformed grains have the same boundary energy and mobility. However, this is not a model restriction, as clear from Eq. (13), but rather a simplification for the lack of data. Eq. (13.f) guarantees that the bubble surface motion is diffusion-controlled. The grain boundary energy and surface energy of UO_2 are taken to be 1.58 $\mathrm{J/m^2}$ and 1.0 $\mathrm{J/m^2}$, respectively [29]. The grain boundary mobility of UO_2 is given by [30]

$$M_{\mathrm{gb}} = 9.21\times10^{-9}\exp(-2.77\mathrm{eV}/K_{\mathrm{B}}T)\,\mathrm{m^4/J\ s} \tag{14}$$

The shear modulus and the magnitude of the Burgers vector for UO_2 are taken as [14] $\mu = 2\times10^{11}\mathrm{J/m^3}$, $b = 0.547\mathrm{nm}$. The interface width was set to be 40 nm in all simulations. A temperature of 1200K is assumed for all the simulations conducted here.

In order to implement this model in MARMOT, a kernel that accounts for the stored energy associated with dislocations has been created. Moreover, an action (called *Polycrystal Stored Energy*) to add this stored energy for each order parameter/grain was also constructed. A Material class (called *Deformed Grain Material*) was also used to specify the dislocation density and model parameters for simulations. Furthermore, All these classes were constructed to be compatible with the Grain Tracker algorithm [31] to reduce the computational cost. Grain Tracker is an algorithm implemented in MOOSE that allows using a few number of order parameters to represent large number of grains, which facilitates performing large scale simulations of polycrystalline materials [31]. The newly added classes take advantage of Grain Tracker to handle both deformed and recrystallized grains. Lastly, the kinetic evolution equations were solved using the same procedure summarized in [28].

3. Results and discussion

We have carried out several 2D simulations for investigating HBS formation in UO_2. We present and discuss the results of these simulations in this section. First, we study the recrystallization in bicrystal systems as a case studies. We then investigate the recrystallization in polycrystalline UO_2. We consider the effect of magnitude and distribution of dislocation density and the presence of bubbles on the process of HBS formation. Simulations of the concurrent recrystallization and bubble formation and evolution were also performed.

3.1 Recrystallization in a bicrystal system

We start here by investigating the recrystallization process in deformed bicrystal systems. These test cases demonstrate the capability of the model on predicting the equilibrium shape of the recrystallized grains and ability to simulate both homogeneous and heterogeneous nucleation. These are major advantages of the model and implementation presented here over the existing models that assume random nucleation and circular shape of the recrystallized grains [19, 20].

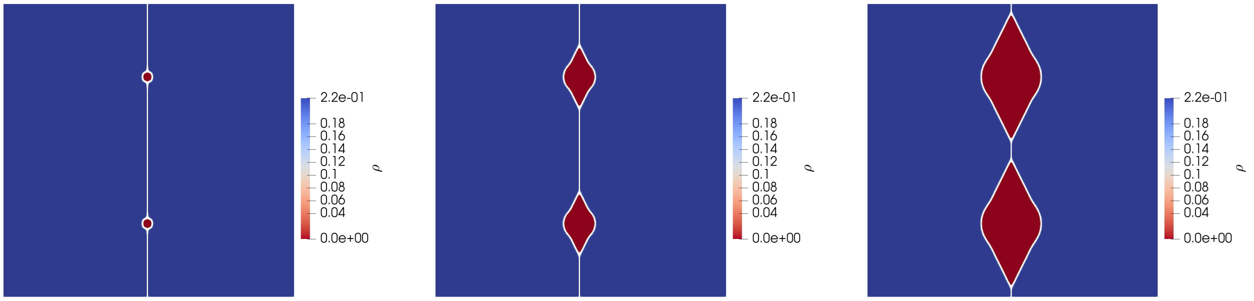

Fig. 7. Growth of two distant recrystallized grains at the grain boundary of a deformed bicrystal. The initially circular grains transform into the equilibrium lenticular shape expected from the mechanical equilibrium condition.

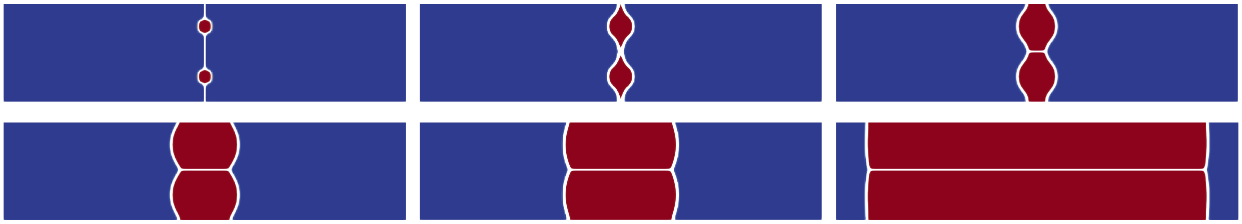

Fig. 8. Growth of two nearby recrystallized grains at the grain boundary of a deformed bicrystal. Initially, the circular grains also quickly assume the equilibrium lenticular shape, but they transform into a rectangular shape after touching and eventually they assume a columnar shape. The shape change is caused by the anisotropic driving force for growth since the recrystallized grains have a driving force to grow only normal to the grain boundary (into the deformed bicrystal).

Two test cases were performed here to study the equilibrium and steady-state shapes of growing recrystallized grains at the boundary of a deformed bicrystal. In the first simulation, two circular recrystallized (dislocation-free) with a radius of 150 nm were placed 512 nm apart from each other at the grain boundary (with a constant dislocation density, $\rho = 2.2 \times 10^{15}\ \mathrm{m}^{-2}$) and the system was allowed to evolve. The system size was 10.24 microns by 10.24 microns and the grid size was 10 nm. The evolution of the system is shown in Fig. 7. It is clear from the figure that, the initially circular grains soon assume the expected equilibrium lenticular shape, which is a result of the requirement of establishing the equilibrium dihedral angle at the triple-junctions to satisfy mechanical equilibrium [25-28]. As also evident from the figure, the recrystallized grains maintain their lenticular shape during growth. However, shape changes during growth may take place when growing grains interact with each other. This is captured in Fig. 8, which shows the growth of two recrystallized grains placed close to each other (just 100 nm apart) on the grain boundary. While the two circular grains also quickly assume the lenticular shape, they then transform into a rectangular and eventually a columnar shape. These morphological changes of the recrystallized grains are due to the fact that upon touching, the boundary between these two grains is flat with zero curvature and thus zero driving force for boundary motion along its normal.

The last case study considered here was dedicated to investigating the nucleation of sub-grains at the grain boundary of a deformed bicrystal. The system size is 10.24 microns by 10.24 microns and the grid size was 10 nm. In contrast to the existing phase-field models of recrystallization [19, 20], no a priori assumptions were made regarding the probability of nucleation or the size and shape of the recrystallizing sub-grains. Instead, the nucleation here was modeled by using 3 extra order parameters reserved for nucleation of new grains. These extra order parameters take a small value between 0.001 and 0.003 assigned using a uniform random number before recrystallization, indicating that no recrystallized grains are present. It has been found that when such a small noise is used, the nucleation behavior is not sensitive to the noise magnitude. However, a rigorous investigation of the nucleation algorithm used is needed and will be done in the short future. Once the dislocation density is high enough, nucleation of recrystallized sub-grains takes place. The critical value of dislocation density for a circular grain with a radius R to grow can be estimated using $\rho^{\mathrm{crit}} = \dfrac{2\gamma_{\mathrm{s}}}{\mu b^2 R}$. At a given dislocation density, this relation gives an upper estimate for the stable nuclei grain radius R.

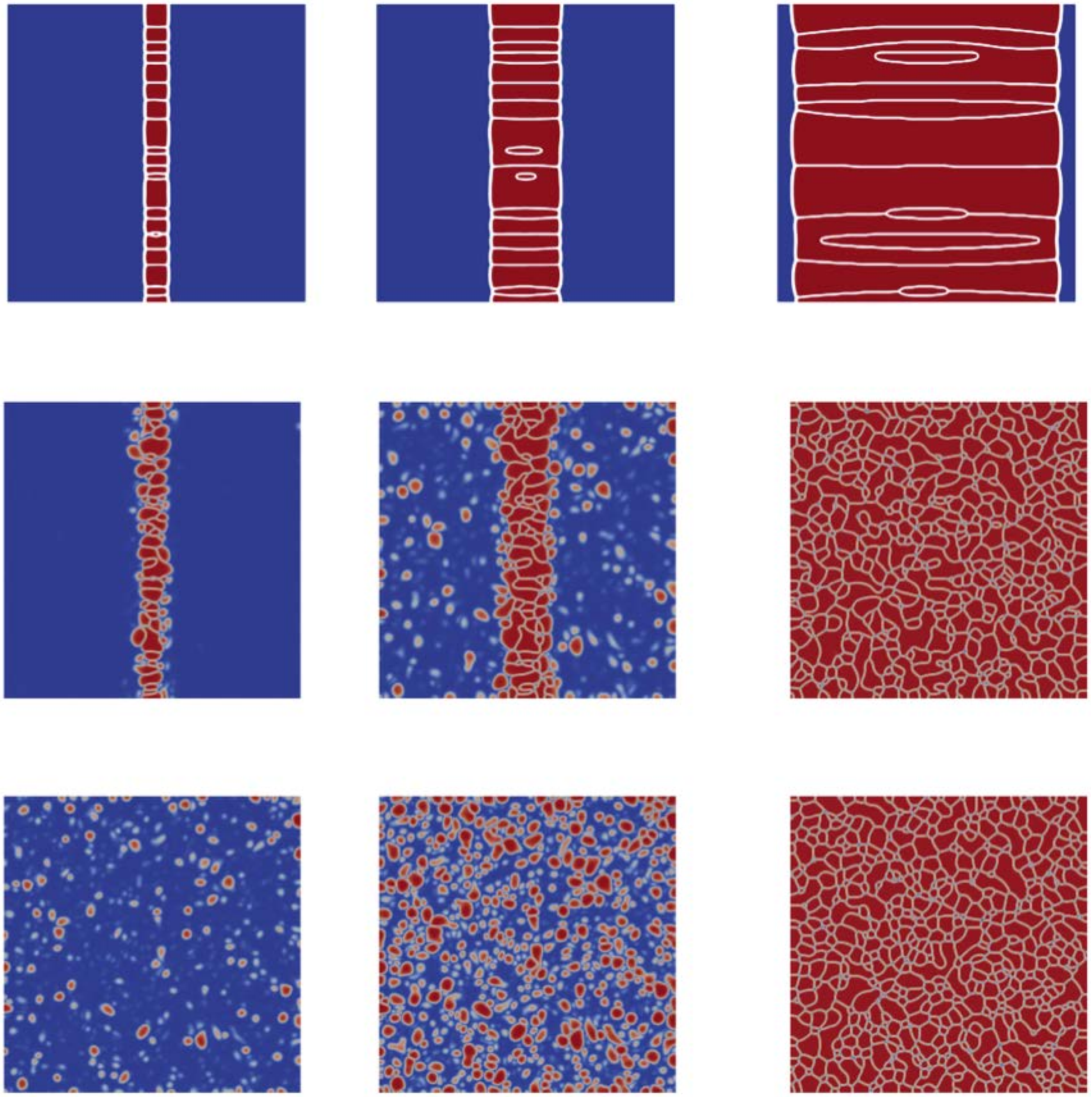

Fig. 9. Effect of dislocation density on the heterogeneous nucleation of sub-grains. For the case of low dislocation density, sub-grains nucleate only at the grain boundary (upper row). For an intermediate value of dislocation density, nucleation of sub-grains starts first at the grain boundary and then in the bulk (middle row). For the case of high dislocation density, sub-grains nucleate everywhere, e.g., homogeneous/uniform nucleation (lower row).

The effect of dislocation density is captured in Fig. 9. The figure presents snapshots of the nucleation and growth of recrystallized sub-grains at different values of dislocation density. For a low value of dislocation density ($\rho = 2.2 \times 10^{15}\ \mathrm{m}^{-2}$), sub-grains nucleate only at the grain boundary since the work of nucleation (and hence the nucleation barrier) there is lower than in the bulk as predicted from heterogeneous nucleation theory [32]. For an intermediate value of the dislocation density ($\rho = 2.8 \times 10^{15}\ \mathrm{m}^{-2}$), recrystallization takes place at the grain boundary first and then in the bulk of the deformed bicrystal. At high value of dislocation density ($\rho = 6.2 \times 10^{15}\ \mathrm{m}^{-2}$), sub-grains nucleate with equal probability everywhere in the domain (homogeneous nucleation). Therefore, the current model is able to simulate both homogeneous and heterogeneous nucleation without any ad hoc or a priori assumptions. We note that in reality as dislocation density builds up from far below the threshold, it is expected that for recrystallization new grains will likely to nucleate from interfaces such as grain boundaries and surfaces. Homogeneous nucleation in grain interior may occur if the initial grain size is large.

3.2 Simulations of HBS formation and evolution

Several 2D simulations of HBS formation and evolution in UO_2 were performed here. First simulations of recrystallization without bubbles are presented. The effects of magnitude and distribution of dislocation density and initial grain size on recrystallization are discussed. Recrystallization in the presence of bubbles was then investigated. Moreover, simulations of concurrent nucleation and growth of both bubbles and sub-grains were also carried out.

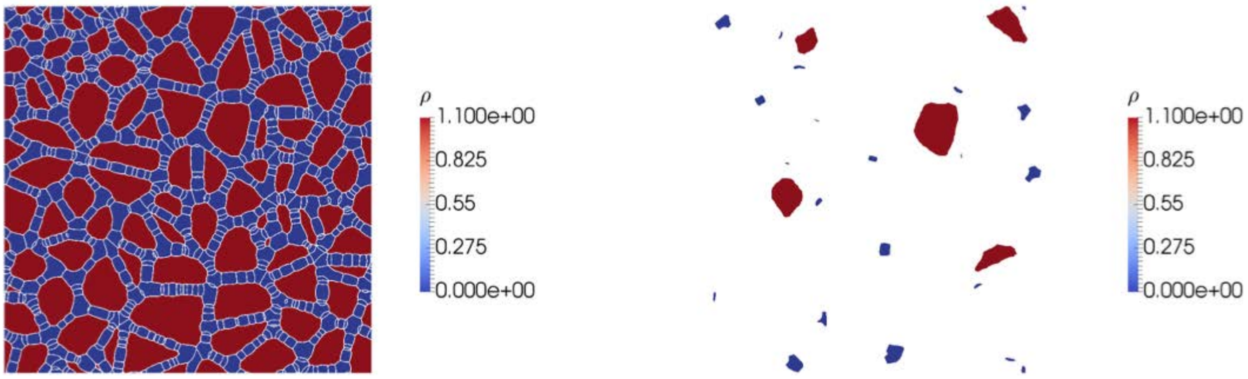

Fig 10. Utilization of grain tracker algorithm to reduce the computation cost. A typical polycrystalline structure (left) with both damaged (in red) and recrystallized (in blue) grains. Assignment of separated grains to a specific order parameter (right) using grain tracker. Note that the grains must be away from each other to prevent unphysical merging, but the same order parameter can be used to represent different deformed and recrystallized grains, reducing the overall computation cost.

The first investigation presented here is on the effect of dislocation density. The system size was 20.48 microns by 20.48 microns with 45 damaged grains initially. The grid size was 10 nm.

All initial grains were assumed to have the same initial dislocation density. As for the bicrystal system, three recrystallized order parameters were reserved for recrystallization of new sub-grains. However, in the polycrystalline simulations presented here, the Grain Tracker algorithm [31] was utilized to handle both the original deformed grains and the recrystallizing grains. Only 9 order parameters (phase fields) were used to represent the initial 45 grains. Moreover, as sub-grains nucleate, the same order parameter can handle both damaged and recrystallized sub-grains as long as they are separated from each other. Such scenario is depicted in Fig. 10. The figure shows that a specific order parameter is being used to describe both deformed and recrystallized grains. In the Grain Tracker algorithm, each grain has a unique ID. By assigning the dislocation density associated with grain ID, multiple grains can use the same order parameter but have different dislocation densities. Furthermore, adaptive time stepping and mesh refinement were used to reduce the computation cost.

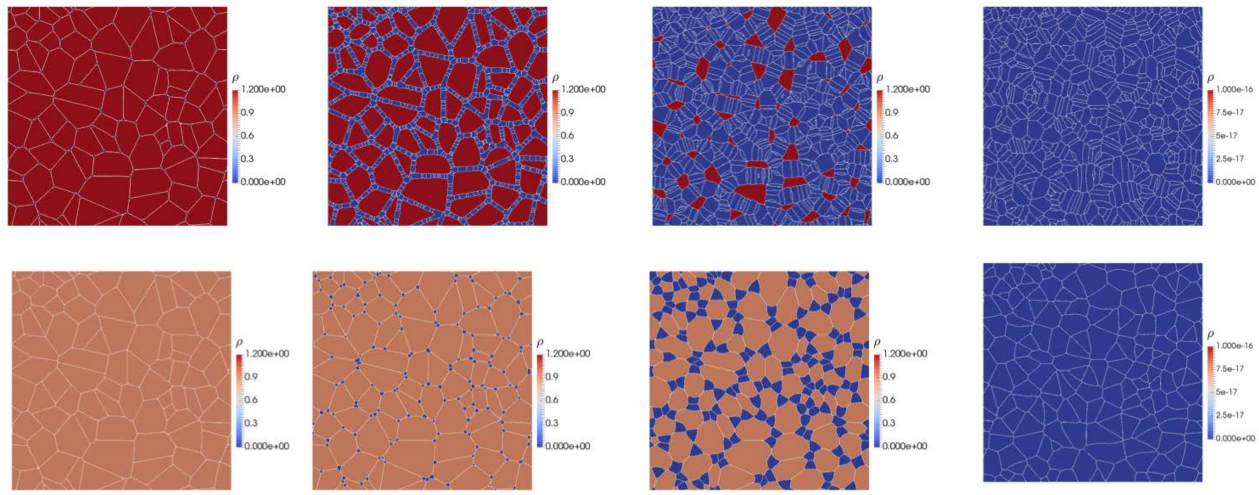

Fig. 11. Effect of dislocation density on the recrystallization in polycrystalline UO_2. For high dislocation density (upper row), sub-grains nucleate on grain boundaries, triple-junctions and higher-order junctions. This dense recrystallization at the boundaries leads to the morphological transformation from lenticular to rectangular to columnar as was shown in Fig. 8 for the bicrystal system. For lower dislocation density (lower row), sub-grains form only at triple- and higher order-junctions. This creates more equiaxed polygonal grains and no metastable columnar structure form.

The effect of dislocation density on the shape and distribution of recrystallized grains is captured in Fig. 11. As evident from the figure, there is a strong effect of the magnitude of dislocation density on the nucleation and morphology of recrystallized grains. For the case of high dislocation density, sub-grains nucleate everywhere on the grain boundaries, which leads to the morphological transformation from equiaxed to columnar as expected before from the bicrystal simulations. On the other hand, sub-grains nucleate only at triple- and higher order-junctions in the case of low dislocation density which leads to the formation of equiaxed grains structure. These predictions are consistent with heterogeneous nucleation theory which anticipates lower nucleation barriers at defects such as grain boundaries and triple junction than in bulk.

The quantitative effect of dislocation density on the recrystallization is presented in Fig. 12. As clear from the figure, higher dislocation density results in faster recrystallization kinetics. Moreover, the average number of recrystallized grains increases with dislocation density, while the average grain size decreases. This also agrees well with predictions from classical nucleation theory since the average number of recrystallized grains is inversely proportional to the driving force of nucleation [32], which here is the strain energy associated with dislocations.

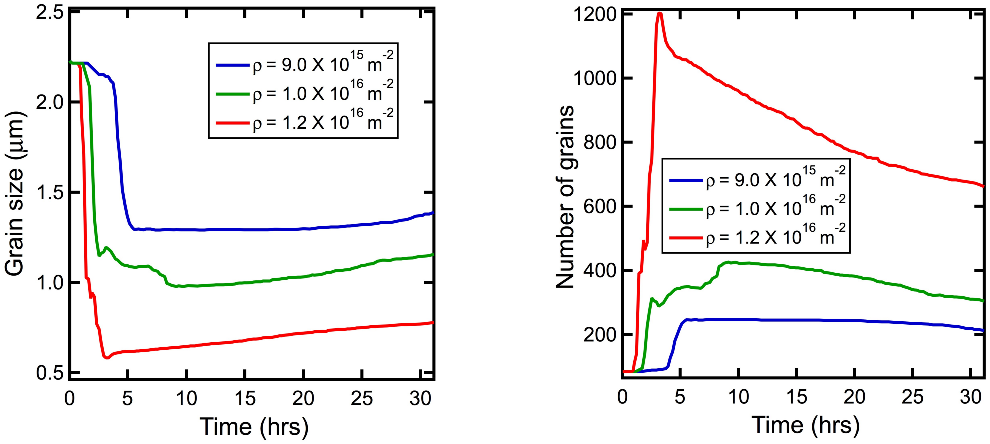

Fig. 12. Effect of dislocation density on grains size (left) and number of grains (right) of recrystallized grains shown in Fig. 11. As the dislocation density increases, the incubation time for nucleation and average grain size of recrystallized grains decrease, while the average number of recrystallized grains increases. Note that after recrystallization is complete, grain growth takes place so that the number of grains decreases and the grain size increases.

Our quantitative results of recrystallization in UO_2 are in reasonably good agreement with other models prediction and experimental data in literature [2-5, 11-15]. As can be seen from Fig. 12, the phase-field model predicts a critical grain size of 0.6-1.3 microns at a critical dislocation density in the range of $\rho = 9\times10^{15} - 1.2\times10^{16}$ m^{-2}, which corresponds to burn-up in the range of 98-105 GWD/tU as calculated from Eq. (12). Most studies reported in average critical burn-up values >60 GWD/tU and local burn-up values >90 GWD/tU [2-5, 11-15]. In fact, according to the recent investigation by Xiao et. al. [14], our predicted values lie within the range of values for the restructuring zone at 1200K as demonstrated in Fig. 13 below. Moreover, the model prediction for the sub-grain size is close to the value of 0.75 microns reported for the same range of burn-up as also shown in Fig. 13. We note that after nucleation, the newly formed grains will grow, driven by either the interfacial energy due to their small size or the strain energy if any deformed grains are in their immediate neighborhood. The strain energy driving grain growth at the expense of deformed grains can also reduce the overall strain energy, directly competing with recrystallization. Therefore, it is critical to have accurate description of grain growth kinetics for HBS, i.e., mobilities for the newly formed grain boundaries, which are very likely over estimated here by using the data for unirradiated UO_2 [30]. The results shown in Fig. 11 and 12 will be re-assessed once more realistic data on grain boundary mobility in HBS is available. An alternative approach is to investigate the effect of grain growth kinetics by performing parametric study. The effect of initial grain size needs to be explored as well for quantitative comparison with experimental data.

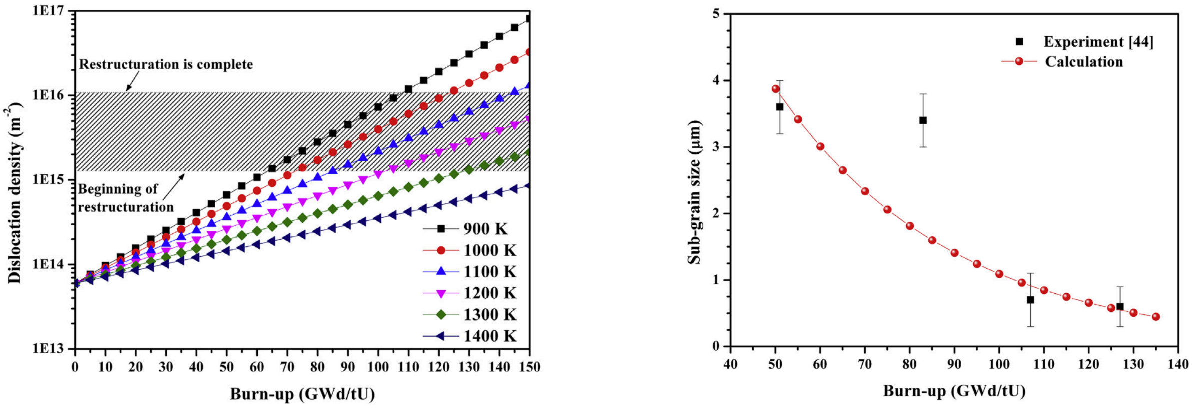

Fig. 13. Critical values of dislocation density and burn-up at which restructuring begins and ends (left) and critical size of sub-grains at different values of burn-up (right) in UO_2 [14]. The figure on the left presents predictions from the fission gas model MARGARET that is capable of describing the restructured zone in UO_2 [14]. The figure on the right is a compilation of results from a rate theory type model and experiments data as appears in [14]. Note that our model results presented in Fig. 12 are in reasonable agreement with the predictions and data presented above.

We then investigated the effect of initial grain size on the recrystallization process in UO_2. The system size was 20.48 microns by 20.48 microns with $\rho = 1.2 \times 10^{16} \mathrm{m}^{-2}$. Two different initial numbers of grains were considered. In the first case, the initial number of damaged grains was 84 with an average grain size of 1.25 microns, and it was 168 in the second case with an average grain size of 0.9 microns. The results are shown in Fig. 14, which shows the number of recrystallized grains with time for these two different samples. As evident from the figure, the sample with larger grain size experience slower recrystallization kinetics. Moreover, the number of recrystallized grains for the sample with lower grain size is higher, which also indicates that the average size of recrystallized grains is smaller. This is consistent with the fact that the sample with smaller grain size has more grain boundary per unit volume and hence more nucleation sites. The trends predicted here for the effect of grain size on recrystallization in UO_2 agree well with the reported experimental data by Nogita et. al. [2]. A step-like recrystallization behavior is noticed in Fig. 13. The exact reason for this behavior is being explored.

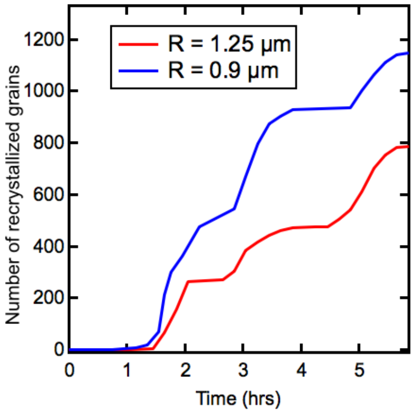

Fig. 14. Effect of initial grain size on the recrystallization process in UO_2. As the initial grain size of damaged grains increases, the number of recrystallized grains decreases. Also, the recrystallization process is faster in the sample with initially smaller grains.

The effect of distribution of dislocation density was also considered. Two simulations were carried out to investigate this effect. In the first simulation, a gradient of dislocation density was assumed across the domain as shown in Fig. 15 to mimic expected distribution across a UO_2 fuel pellet in light water reactors (LWRs). As shown in the figure, the non-uniform distribution of dislocation density results in heterogeneous nucleation of sub-grain as they form first in regions of high dislocation density. Moreover, it leads to non-uniform grain morphologies, i.e., grains in the high dislocation density region form everywhere on the boundaries and develop columnar structure, while grains in the low dislocation density region form only at triple- and higher order-junctions and develop more equiaxed structures. The second simulation, on the other hand, was designed to mimic expected distribution of dislocation density in MOX fuels where $(U,Pu)O_2$ agglomerates are usually randomly distributed. It is anticipated that dislocation density will be higher in the vicinity of these agglomerates. This scenario is depicted in Fig. 16 that presents snapshots of the recrystallization process in such system. Heterogonous nucleation of sub-grains is observed in this situation as well where formation of new grains is only confined to regions with high dislocation density. Again, we note that the grain growth kinetics after recrystallization might have been overestimated as in the case of Fig. 12.

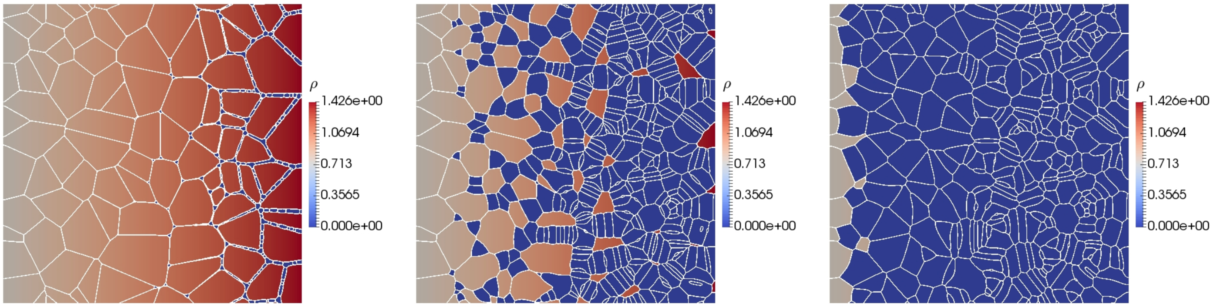

Fig. 15. Effect of expected distribution of dislocation density in UO_2 fuel pellet in LWRs on recrystallization (ρ is in units of $\times 10^{16}\mathrm{m}^{-2}$). A positive gradient in dislocation density is created from the left to the right to mimic the expected gradient from the center to the rim of a fuel pellet. Heterogonous nucleation of sub-grains takes place from the right boundary where the dislocation density is high. Moreover, the dislocation density gradient results in non-uniform morphology of grains since grains in the high dislocation density region develop columnar structure, while grains in the low dislocation density region assume equiaxed polygonal structure.

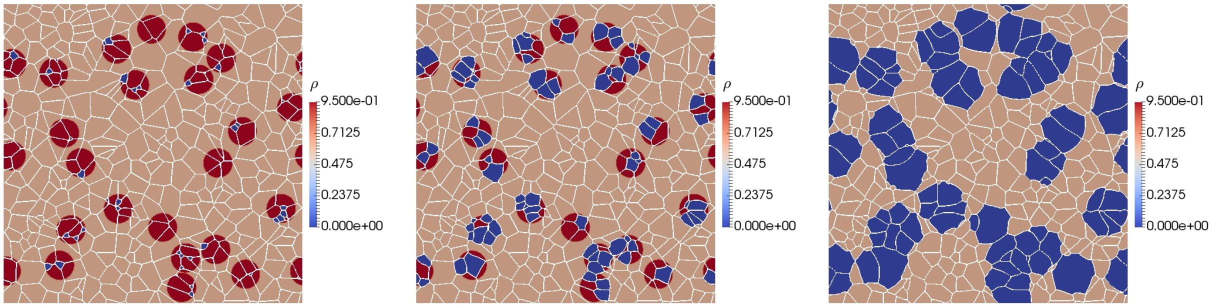

Fig. 16. Effect of expected distribution of dislocation density in MOX fuel pellet on recrystallization (ρ is in units of $\times 10^{16}\mathrm{m}^{-2}$). It is assumed that the dislocation density is higher in the vicinity of $(U,Pu)O_2$ agglomerates, which are distributed randomly. Heterogeneous nucleation of sub-grains is also observed here, where sub-grains only nucleate in regions of high dislocation densities.

The last few simulations discussed here are dedicated to investigating the effect of bubbles on the recrystallization process and concurrent formation and evolution of sub-grains and bubbles. First the effect of bubbles on the recrystallization process was studied using a simplified hexagonal grain structure with a central bubble. Moreover, it was assumed that the surface energy doubled the grain boundary energy. While this is not the case for UO_2 (recall the UO_2 parameters in section 2), this assumption was made here to make the comparison of simulation to predictions from heterogeneous nucleation clearer. In such situation, according to heterogeneous nucleation theory, nucleation will take place first at the bubble surface, then triple-junction, then grain boundary, and finally in the bulk as the dislocation density increases. This trend was indeed obtained from the simulation shown in Fig. 17. The figure presents snapshots of the formation of sub-grains at different dislocations densities. The system size was 10.48 microns by 10.48 microns and the central bubble radius was 1 micron. The dislocation density increased in the simulations shown from top to bottom. Specifically, the dislocation densities from the top to the bottom rows are $\rho = 4.0\times10^{15}\mathrm{m}^{-2}$, $\rho = 5.0\times10^{15}\mathrm{m}^{-2}$, $\rho = 9.0\times10^{15}\mathrm{m}^{-2}$, and $\rho = 2.0\times10^{16}\mathrm{m}^{-2}$, respectively. Note that the recrystallizing sub-grains assumed different shapes depending on where they form. This is a manifestation of the mechanical equilibrium conditions that requires the establishment of an equilibrium dihedral angle at triple-junctions (sub-grains tips). The prediction of these different shapes is a major advantage of the current model over the existing phase-field models that assume circular shape of recrystallized sub-grains [19, 20].

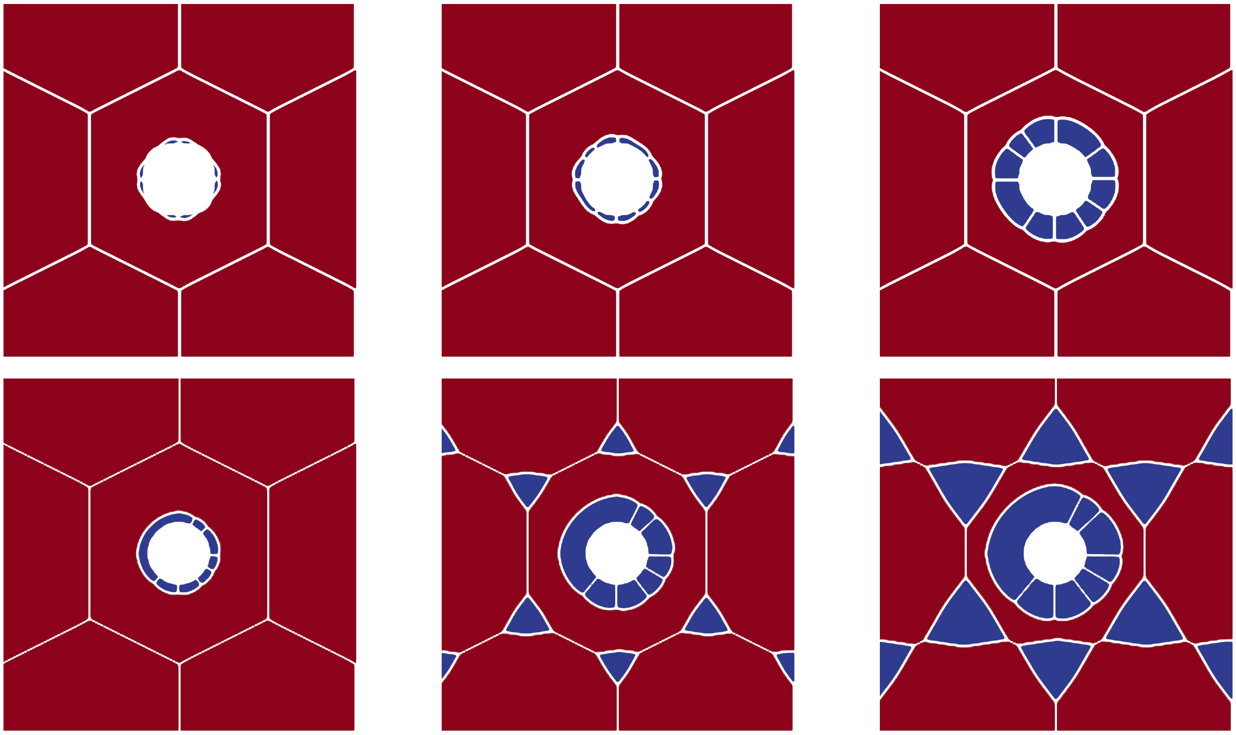

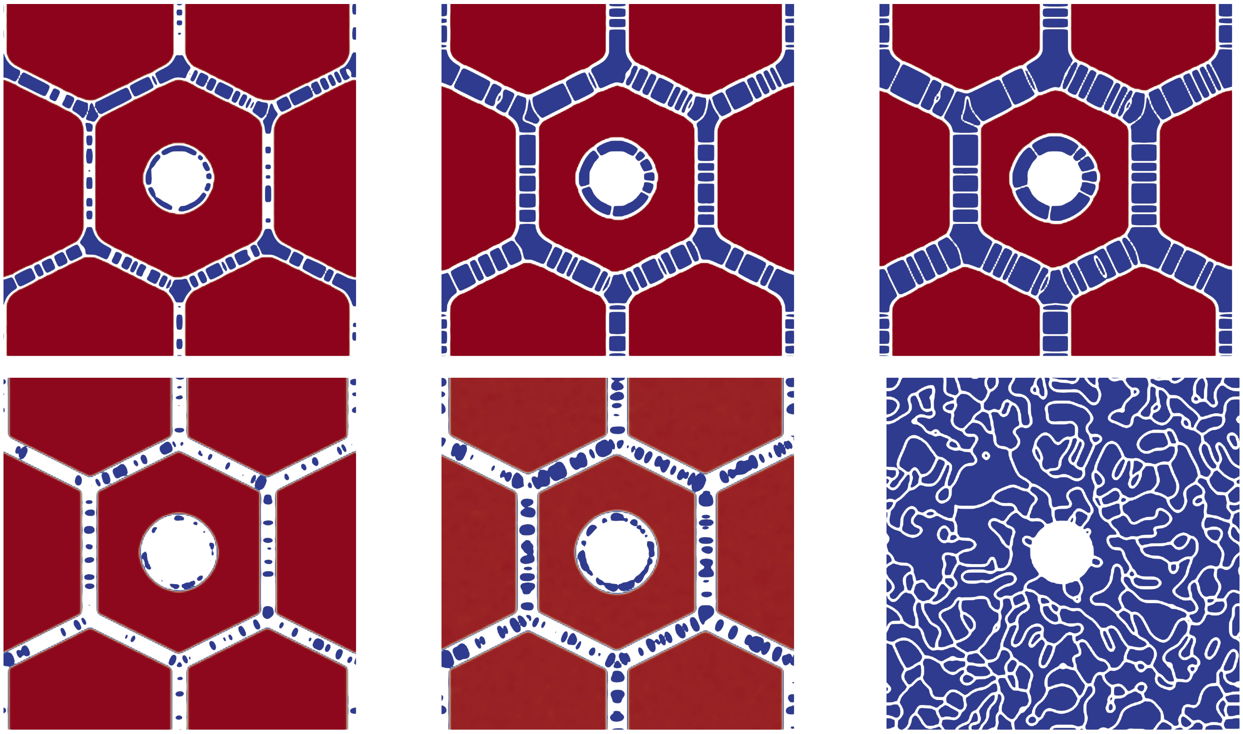

Fig. 17. Effect of dislocation density and ratio of bubble surface energy to grain boundary energy on the recrystallization process in a deformed hexagonal structure containing a central bubble. The surface to grain boundary ratio assumed here to be 2.0. The dislocation density increase from top to bottom (see text for exact values). For such system, nucleation starts at bubble surface, then triple-junctions, then grain boundaries and lastly in the bulk with increase of dislocation density in agreement with predictions from heterogeneous nucleation theory [32].

A more realistic polycrystalline structure with the actual ratio of surface to grain boundary energy of UO_2 (0.633) was considered next. The system size was 20.48 microns by 20.48 microns with 50 deformed grains and 50 randomly distributed bubbles of 150 nm radius. Snapshots of the formation and growth of sub-grains in this system are presented in Fig. 18. Note that sub-grains here tend to form first at triple- and higher order-junctions then grain boundaries and bubble surfaces, which is consistent with the fact that grain boundary energy is higher than surface energy in UO_2. It is also important to note the shapes of the recrystallized sub-grains around the bubble surface. These sub-grains tend to first grow parallel to (wrap around) the bubble surface before growing into the deformed bulk grains. In some situations when only one grain nucleates at a bubble surface, the formed sub-grain assume a complete round shape around the bubble. The formation of such round sub-grains around bubbles is reported in literature [3, 10]. It is also worthy to point out that the shapes of bubbles change after nucleation of sub-grains at their surface. This is again to satisfy mechanical equilibrium at the bubble triple-junctions (tips).

Lastly, the concurrent formation and growth of bubbles and sub-grains was investigated. Here, the accumulation of both Xe gas atoms and dislocations with time due to fission events was directly considered. A fission rate of $\dot{f} = 4\times10^{19}\,\mathrm{m^{-3}s^{-1}}$ was assumed. The production rate of Xe was then taken to be $1\times10^{19}\,\mathrm{m^{-3}s^{-1}}$ and the accumulation of dislocation density was assumed to follow the exponential form, $\rho(t) = \rho(0)\exp(A\cdot\dot{f})t$, where $A = 2\times10^{-27}\,\mathrm{m^3}$ and the initial dislocation density is assumed $\rho(0) = 6\times10^{13}\,\mathrm{m^{-2}}$ [14]. In order to reduce computation cost, a hexagonal structure with periodic boundary conditions was used. The evolution of the system is presented in Fig. 19, which shows snapshots of the formation and growth of both bubbles and sub-grains. As clear from the figure, bubbles tend to form first before sub-grains. Moreover, bubbles nucleate first at triple-junctions and then at grain boundaries in agreement with heterogeneous nucleation theory [32]. Sub-grains then form at bubble surfaces. Furthermore, due to the on-going production of Xe gas atoms, new bubbles form at the boundaries of recrystallized grains. In other words, formation of bubbles facilitates recrystallization of sub-grains, which in turn facilitates the formation of new bubbles and growth and coarsening of existing ones.

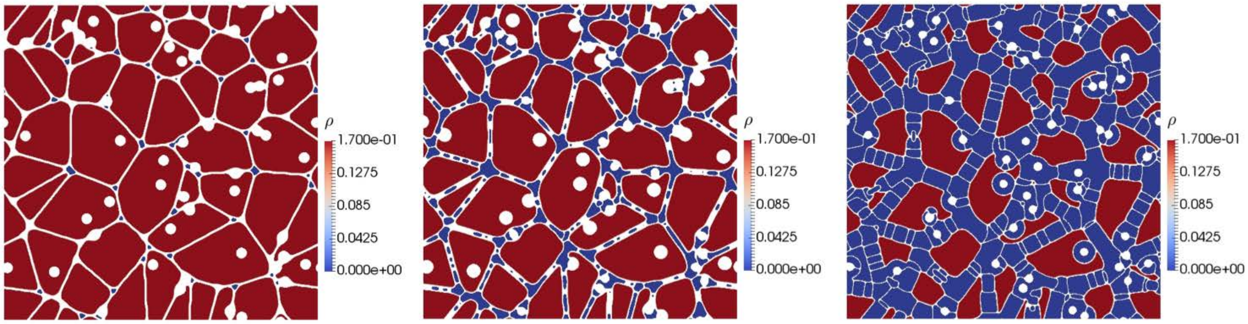

Fig. 18. Snapshots of the recrystallization process in UO_2 in the presence of bubbles. Since grain boundary energy is higher than surface energy, sub-grains form first at triple- and higher-order-junctions, then grain boundaries and then bubble surface. Note the rounded shape of sub-grains nucleated at the surface of some bubbles. The bubbles shape also changes after the nucleation of sub-grains to maintain mechanical equilibrium at bubble tips.

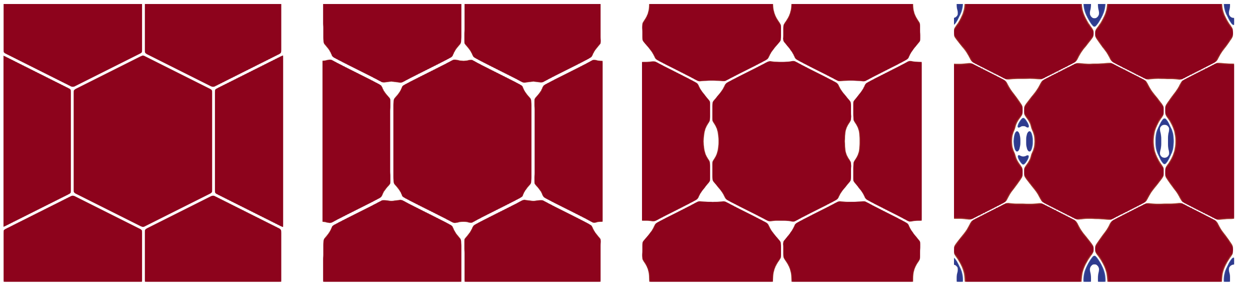

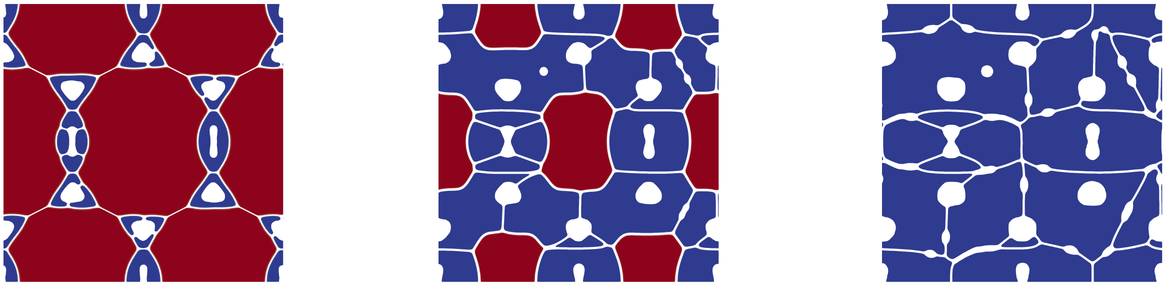

Fig. 19. Snapshots of concurrent bubble and sub-grains formation and growth in UO_2. Bubbles form first at triple-junctions and then at grain boundaries. Sub-grains then form at bubble surfaces. The same surface energy and grain boundary energy as in Fig. 17 are used here. Moreover, new bubbles nucleate at the boundaries of recrystallized sub-grains.

4. Discussion

4.1 Quantification of driving forces

The present model is based on the hypothesis of dislocation driving recrystallization for HBS formation. The driving force is the strain energy that is induced by the dislocations and loops that are formed by production and accumulation of radiation damage. Therefore, it is critical to have a quantitative model describing how the dislocation density evolves during fuel operation, and that describing the strain energy as a function of dislocation density and possibly loop sizes. Currently, an empirical model [15] that is fitted to a set of experimental data is used for the evolving dislocation density, and a simple model as shown in Eq. (4) is used to estimate the strain energy. A couple of other empirical models also exist in the literature [11-14]. The empirical nature of these models limits their usage in a wide range of operation conditions and new fuel types. Physics-based models for radiation damage evolution are highly desired for HBS formation and many other aspects of microstructure evolution in fuels. Such an effort has been initiated in FY17 using cluster dynamics modeling. The model is adapted from a literature model for predicting the evolution of dislocation loops and voids in pure Fe [33]. The schematic of the modeling approach is shown in Fig. 20(a). In our modeling, fission events create dense cascades which lead to the production of interstitials and vacancies and their clusters. Since U defects are rate-limiting diffusion species, we assume the evolution of microstructures is governed by U interstitials and vacancies. The defects produced from cascades can have in-cascade recommendation, be annihilated by dislocations (dislocation bias is considered), aggregate to form interstitial-type dislocation loops with a disk shape and voids with a spherical shape, and recombine between opposite-type defects/clusters. The interstitial loops and vacancy clusters can thermally emit defects and the emission rates are based on their respective size-dependent defect cluster binding energy models. Here the dislocation loops are assumed to have a lower binding energy than vacancy clusters at the same cluster size. As the first step, only mono interstitials and mono vacancies are considered to be diffusive. The diffusivities of U vacancies and interstitials are taken from previous DFT calculations [34]. Specifically, the U vacancy diffusion coefficient is $D_v=7.12\times10^{-7}\exp(-4.72\ \text{eV}/k_BT)\ \text{m}^2/\text{s}$, and that of U interstitial is $1.2\times10^{-6}\exp(-3.05\ \text{eV}/k_BT)\text{m}^2/\text{s}$. We use this modification to take the fast interstitial cluster diffusion into account. The fuel irradiation temperature is set to 1000 K, which is within the fuel rim temperature range in Ref. [35]. The initial dislocation density is $6\times10^{13}\ \text{m}^{-2}$ according to Ref. [35], where the irradiation dose rate is unclear. According to Ref. [1], LWR fuels receive about 1 dpa/day of irradiation and HBS starts to form at 50 GWd/t after a 4-year irradiation time. Therefore, the dose rate is estimated at about 1 dpa/day, which is equivalent to 0.034 GWd/t/day.

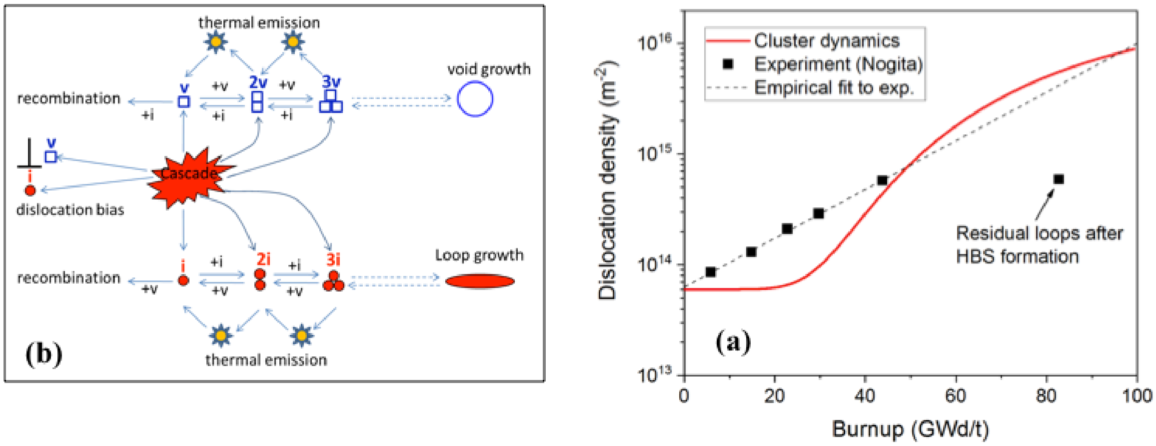

Fig. 20. Cluster dynamics modeling of dislocation loop evolution in UO_2 fuels. (a) Schematic of cluster dynamics modeling framework. (b) The evolution of dislocation density as a function of fuel burn-up under typical LWR conditions.

The evolution of dislocation loop density as a function of fuel burn-up from cluster dynamics modeling is shown in Fig. 20(b). The volumetric dislocation loop density (N_{loop}) from our modeling is converted to area density (ρ_d) through $\rho_d = \pi dN_{loop}$, where d is loop diameter. Since in experiments TEM has a resolution limit, here we assume only loop diameter greater than 2 nm (~ 30 UO_2 molecules) are detectable and can be counted in the dislocation density. Therefore, Fig. 20(b) only shows the density of dislocation loops that contain more than 30 U interstitials. From the cluster dynamics modeling, the dislocation loop density remains nearly constant up to the local burn-up of 20 GWd/t. Then the loop density increases monotonically with fuel burn-up. During this stage, the loop coarsening dominates the evolution. In the experimental data, the common logarithm of dislocation density increases almost linearly with the burn-up up to 50 GWd/t. Above this burn-up, the HBS starts to form so the dislocation density remains nearly constant. Therefore, if HBS would not form, the dislocation density should keep increasing, as the dashed line shows. Compared with experimental trend, overall the modeling captures the correct loop evolution trend (i.e., loop density increases with burn-up). However, our model underestimates the dislocation density when the burn-up is below 50 GWd/t and slightly overestimates the dislocation density above 50 GWd/t. Therefore, there is some room for further improvement of our model if we assume the experimental data reported in Ref. [35] is reliable. One potential improvement area is to directly include the interstitial cluster diffusion in the modeling, which may help capture the fast loop growth feature at low burn-up. The other potential improvement is to conduct sensitivity analysis to determine how the results are sensitive to different input parameters. The effect of grain size needs to be considered as well. These improvements will be conducted in our next phase of study.

Along with the formation of HBS are the segregation and/or precipitation of fission products, including fission gases and solid fission products, in the newly formed grain boundaries. This may also contribute to the driving force for HBS formation, and it can be substantial since the densities of these impurities can be high at high burn-up. The free energy expression as given in Eqs. (3) and (6) can be extended to include this driving force, provided that the evolution and thermodynamics of fission products are known. Modeling the evolution of fission products is within the NEAMS scope.

The current model describes HBS formation as a recrystallization process. Some other mechanisms have also been proposed. With the same driving force of strain energy, HBS may also occur via grain subdivision, i.e., the self-organization of dislocations into low-angle grain boundaries which divide the original grains into sub-grains [1]. Although the preliminary results from the present model indicate that it's promising in predicting HBS formation, further model development is possible after better understanding of HBS formation mechanism is achieved.

4.2 Grain growth in HBS

After formation, HBS has been shown to have an averaged grain size which is stable under both irradiation and annealing, in contrast to Fig. 12 which shows increasing grain size after fully recrystallized. This discrepancy comes from two possible reasons. First, in the simulation shown in Fig.12 the dislocation density is set to be zero in recrystallized grains without further building-up. On the other hand, thermal and strain driving grain growth is still on-going which increases the overall grain size. During fuel operation, radiation damage is produced continuously in both original and recrystallized grains. Under such a condition, it is expected that recrystallization and grain growth take place simultaneously, and the dynamic competition between them will stabilize a steady state grain size. Second, in the present model the mobility used is derived from grain growth experiments in fresh UO_2. While in HBS, the grain boundaries in recrystallized regions are decorated with gas bubbles, intermetallic precipitates and segregated impurities. The effective mobility can be orders lower due to second phase particle pinning and solute dragging. Effectively grain growth can be suppressed or slowed down at relatively high temperatures.

These two limitations will be resolved in a short future. Actually, as a dislocation evolution model as in Eq. (12) has already been implemented, dynamic simulations with simultaneous recrystallization and grain growth can be carried out using the current model. This will be performed in FY18, with the expectation that steady state grain sizes will be reached at given conditions combining fission rates and temperature. The motion of grain boundary with particle pinning has been already captured well by MARMOT [28]. The effect of solute dragging on grain boundary mobility in UO_2 will be explored too under NEAMS. With these capabilities, a more realistic description of grain growth behavior in recrystallized regions can be obtained in MARMOT.

4.3 Developing materials models to be used at the engineering scale

The mesoscale model developed in MARMOT can be used to directly simulate HBS formation under various conditions and to demonstrate the simultaneous evolution of grain structure and gas bubbles. A more important purpose of this development is to use mesoscale simulations to develop materials models that can be used in engineering scale fuel performance modeling, such as in BISON. Ideally, theses models will describe the evolving fuel microstructure that is defined by a list of state variables [36], tentatively including grain size, porosity and concentrations of fission products. Meanwhile, structure-property correlations are needed to predict the transient fuel properties in HBS such as thermal conductivity and mechanical strength. The exact forms of these models to be developed will be worked out once the mesoscale model for HBS is mature to allow for simulations with large number of grains and high burn-up.

5. Conclusion

A novel phase field model for high burn-up structure formation and evolution was introduced. The model directly accounts for the chemical energy of gas atoms, interfacial energies of grain boundaries and bubble surfaces, and strain energy associated with dislocations, which renders the model capable of simulating the concurrent formation and growth of both bubbles and sub-grains. Moreover, in contrast to existing phase-field models of recrystallization, the current model simulate the nucleation stage directly and no ad hoc or a priori assumptions are required for the nucleation rate or recrystallized grain size and shape. It also has the advantage of simulating concurrent recrystallization and fission gas bubble formation. All the model parameters were quantified in terms of thermodynamic and kinetic properties. The model has been numerically implemented in MARMOT. The implementation utilizes the Grain Tracker algorithm [31] to reduce computational cost.

The model was shown to be able to simulate homogeneous and heterogeneous nucleation of both bubbles and sub-grains. Bubbles and recrystallized grains tend to form first at triple- and higher order-junctions then grain boundaries and then in the bulk in agreement with predictions from heterogeneous nucleation theory [32]. Moreover, sub-grains also nucleate at the surfaces of bubbles. Furthermore, new bubbles form on the boundaries of recrystallized sub-grains due to the on-going production of gas atoms. The simulations presented here clearly demonstrate that the nucleated sub-grains and bubbles assume different shapes at different nucleation locations as reported in experiments [2-10]. This is a manifestation of the mechanical equilibrium condition that translates into the establishment of equilibrium dihedral angles at the sub-grains and bubbles tips. Preliminary results from simulations in polycrystalline UO_2 suggest a threshold dislocation density for the HBS formation at 1200K of about $\rho = 9\times10^{15} - 1.2\times10^{16}\ \mathrm{m}^{-2}$, which corresponds to burn-up in the range of 98-105 GWD/tU. The recrystallized average grain size was found to be on the order of 0.6-1.3 microns. These values lie well within the range of reported data in literature [14]. Although the simulations shown here are 2D for the purpose of demonstration, the current model can be used for 3D simulations, which will require high computation cost when large numbers of grains are involved. As in 3D the competition between strain energy and interfacial energy can be slightly different from that in 2D, 3D simulations will be performed in the future to investigate HBS formation in a more realistic manner.

The model will be further refined as discussed in the Discussion Section, and will be used to perform mesoscale simulations for HBS formation with the purpose of developing materials models to be used in the engineering scale fuel performance modeling.

References

[1] V. Rondinella and T. Wiss, Materials Today 13, 24 (2010).
[2] K. Nogita, K. Une, M. Hirai, K. Ito, Y. Shirai, Journal of Nuclear Materials 248, 196 (1997).
[3] J. Spino, K. Vennix, M. Coquerelle, Journal of Nuclear Materials 231, 179 (1996).
[4] M. Cumningham, M. Freshley, D. Lanning, Journal of Nuclear Materials 188, 19 (1992).
[5] K. Une, M. Hirai, K. Nogita, T. Hosokawa, Y. Suzawa, S. Shimizu, Y. Etoh, Journal of Nuclear Materials 278, 54 (2000).
[6] K. Une, K. Nogita, T. Shiratori, K. Hayashi, Journal of Nuclear Materials 288, 20 (2001).
[7] A. Romano, M. Horvath, R. Restani, Journal of Nuclear Materials 361, 62 (2007).
[8] J. Noirot, L. Desgranges, J. Lamontagne, Journal of Nuclear Materials 372, 318 (2008).
[9] J. Noirot, J. Lamontagne, N. Nakae, T. Kitagawa, Y. Kosaka, T. Tverberg, Journal of Nuclear Materials 442, 309 (2013).
[10] Y. Kim, G. Hofman, J. Cheon, Journal of Nuclear Materials 436, 14 (2013).
[11] J. Rest and G. Hofman, Journal of Nuclear Materials 210, 187-202 (1994).
[12] J. Rest, Journal of Nuclear Materials 346 (2–3), 226-232 (2005).
[13] J. Rest, Journal of Nuclear Materials 349 (1-2), 150-159 (2006).
[14] H. Xiao, C. Long and H. Chen, Journal of Nuclear Materials 471, 74-79 (2016).
[15] K. Nogita and K. Une, Journal of Nuclear Materials 226, 302-310 (1995).
[16] N. Provatas and K. Elder, Phase-Field Methods in Materials Science and Engineering. (Wiley-VCH, Weinheim, Germany, 2010).
[17] H. Emmerich, Adv. Phys. 57, 1 (2008).
[18] N. Moelans, B. Blanpain and P. Wollants, Physical Review B 88, 054103(2013).
[19] S. Gentry and K. Thornoton, IOP Conf. Series: Materials Science and Engineering 89, 012024, (2015).
[20] L. Liang, Z. Mei, Y. Kim, B. Ye, G. Hofman, M. Anitescu, A. Yacout, Computational Materials Science 124, 228, (2016).
[21] N. Moelans, B. Blanpain, and P. Wollants, Physical Review B 78, 024113 (2008).
[22] N. Moelans, Acta Mater 59, 1077 (2011)
[23] L. Amirouche and M. Plapp, Acta Mater 57, 237 (2009)
[24] M. Plapp, Physical Review E 78, 031601 (2011).
[25] K. Ahmed, C. Yablinsky, A. Schulte, T. Allen and A. El-Azab, Modelling and Simulation in Materials Science Engineering 21, 065005, (2013).
[26] K. Ahmed, J. Pakarinen, T. Allen, and A. El-Azab, Journal of Nuclear Materials 446, 90, (2014).
[27] K. Ahmed , T. Allen, and A. El-Azab, Journal of Materials Science 51, 1261, (2016).
[28] K. Ahmed, M. Tonks, Y. Zhang, B. Biner, and A. El-Azab, Computational Materials Science 134, 25, (2017).
[29] P.V. Nerikar, K. Rudman, T.G. Desai, D. Byler, C. Unal, K.J. McClellan, S. Phillpot, S. Sinnott, P. Peralta, P. Uberuaga, and C. Stanek, Journal of the American Ceramic Society 94,1893–1900 (2011).
[30] J.B. Ainscough, B.W. Oldfield, and J.O. Ware, Journal of Nuclear Materials 49 (2), 117-128 (1973).
[31] C. Permann, M. Tonks, B Fromm, and D. Gaston, Computational Materials Science 115, 18-25 (2016).
[32] R. Bullafi, W. Carter and S. Allen, Kinetics of Materials. (Wiley, 2005).
[33] R.E. Stoller et al., Journal of Nuclear Materials 382, 77 (2008).
[34] D. A. Andersson et al., JNM 462, 15 (2015).
[35] K. Nogita and K. Une, NIMB 91, 301 (1994).
[36] M. R. Tonks, D. Andersson, S. R. Phillpot, Y. F. Zhang, R. Williamson, C. R. Stanek, B. P. Uberuaga, and S. L. Hayes, Annals of Nuclear Energy 105: 11–24 (2017).